Natural sloshing frequencies and modes in a rectangular tank with a slat-type screen

O.M. Faltinsen *, A.N. Timokha

Centre for Ships and Ocean Structures, Department of Marine Technology, Norwegian University of Science and Technology, NO-7491 Trondheim, Norway

ARTICLE INFO

ABSTRACT

Being installed in tanks, screens play the role of slosh-suppressing devices which may strongly change resonant sloshing frequencies and yield an extra nonlinear damping due to cross-flow resulting in either flow separation or jet flow. Employing the linear sloshing theory and domain decomposition method, we construct an accurate analytical approximation of the natural sloshing modes in a rectangular tank with a slat-type screen at the tank middle. Two-dimensional irrotational flow of an ideal incompressible liquid is assumed. Because the considered flow model does not account for flow separation and jet flow at the screen, the velocity field is locally singular at the sharp edges. The constructed solution captures this singularity. Analyzing this solution establishes a complex dependence of the natural sloshing frequencies on the solidity ratio, the number of submerged screen gaps, the liquid depth, and the position of perforated openings relative to the mean free surface. Results are compared with experimental data. Natural surface wave profiles are discussed in the context of a jump of the velocity potential at the screen and the local inflow component to the screen.

© 2010 Elsevier Ltd. All rights reserved.

1. Introduction

Screens and perforated plates are well known as efficient tools for suppressing the resonantly forced sloshing. Their applicability has been studied in the past century in the context of liquid sloshing in fuel rockets tanks [1]. Other applications are associated with anti-rolling tanks of ships, tuned liquid dampers (TLD) of tall buildings, swash bulkheads of ships, and perforated plates of oil–gas separators on floating platform. Anti-rolling tanks and TLDs can be either free-surface tanks or U-tube. Our focus is on free-surface tanks. A review can be found in the textbook [2, Chapter 1].

The solidity ratio $0 \le \mathrm{Sn} \le 1$, i.e. the ratio of the area of the shadow projected by the screen on a plane parallel to the screen to the total area contained within the frame of the screen, is an important flow parameter of screens. The value $\mathrm{Sn}=0$ means no screen (henceforth, the *clean* tank), and $\mathrm{Sn}=1$ indicates that the screen becomes a rigid wall. A design requirement for anti-rolling tanks and TLDs is that the lowest resonant sloshing frequency of a screen-equipped tank should be close to the roll natural sloshing frequency and the most important structural natural frequency, respectively. The consequence is that either the wave-induced roll motions of a ship or wind- and earthquake-excited vibrations of tall buildings are clearly reduced. Because it is desirable with the highest possible damping of sloshing with a negligible change of the lowest resonant sloshing frequency, a rough guideline for a free-surface tank is that $\mathrm{Sn} \approx 0.5$. The objectives for a swash bulkhead in cargo liquid tanks of ships and perforated plates in oil–gas separators on floating platforms are to provide sloshing damping as well as to change the lowest resonant sloshing frequency to a higher frequency range where

* Corresponding author.
   E-mail address: odd.faltinsen@ntnu.no (O.M. Faltinsen).

the wave-induced ship and platform velocities and accelerations are less severe. The consequence is a high solidity ratio. However, the optimum solidity ratio is *not* the highest Sn=1.

To describe the resonantly forced sloshing and estimate the corresponding resonant frequencies, i.e. the forcing frequencies where a local maximum of the free-surface elevations occurs, we have to account for free-surface nonlinearity and for either flow separation or jet flow through the screen. The latter leads to a quadratic damping in the mechanical system which implies that the resonant response has a quadratic dependence on the forcing amplitude (see, [2, Chapters 6; 3,4] and references therein). The quadratic damping due to either flow separation or jet flow as well as the free-surface nonlinearity may cause a change of the resonant frequencies relative to the natural sloshing frequencies which can be considered as an asymptotic limit of the resonant frequencies when the forcing amplitude tends to zero. In other words, the natural sloshing frequencies are not the same as the resonance frequencies with a finite lateral tank forcing. However, they give the lowest-order prediction for the occurrence of resonance peaks of the steady-state response curves in terms of the forcing amplitude.

In general, the linear sloshing theory for tanks with internal structures yields the natural sloshing modes and frequencies which differ from those for the clean tank. A review on how a rigid submerged 'small-volume' structure (in particular, a screen) may change the natural sloshing frequencies and modes can be found in the textbook [2, Chapter 4]. In the present paper, we study a changing of the *natural* sloshing frequencies and modes due to a slat-type screen in a rectangular tank without accounting for either flow separation or jet flow at the openings, namely, the nonlinear phenomena due to the screen are neglected. To the best of authors knowledge, the literature contains *neither analytical nor numerical studies* of the natural sloshing frequencies and modes for tanks with a slat-type screen. The present paper is novel for this problem.

Ideal incompressible liquid with irrotational flow is assumed. The linear two-dimensional sloshing problem with finite liquid depth is considered. The slat-type screen appears as a perforated vertical plate installed at the tank middle. The screen divides the unperturbed liquid volume into two equal compartments with openings allowing for a cross-flow. The mathematical statement is presented in Section 2. It is associated with the well-known spectral boundary problem [2, Chapter 4] with additional transmission conditions at the screen. Even (symmetric) natural sloshing modes of the corresponding clean rectangular tank remain a solution of this problem. However, odd (antisymmetric) modes do not satisfy the transmission conditions. Using a domain decomposition method similar to that in [5–7], we construct an integral representation of the natural sloshing modes as a function of the normal velocity at the screen openings. Finding the antisymmetric natural modes leads to a system of homogeneous integral equations with respect to these normal velocities. The spectral parameter of the original boundary problem (representing the natural sloshing frequencies) should be found from the solvability condition of this system. The constructed system is solved in Section 3 by a Galerkin method. The solution procedure involves coordinate functions which capture local asymptotics of the normal velocity at the sharp edges of the slats. There is a similarity between the proposed formulation and solution method and that used by Porter and Evans [5] for wave scattering problem, although they did not apply their method to multiple gaps. A difference is the chosen set of coordinate function. Evans and Porter (and many authors thereafter) use an orthogonal set of functions containing the required singular behavior at the edges of the gaps which may be integrated explicitly. In contrast, we use a nonorthogonal set of functions, which have the same effect of allowing integrals to be done explicitly.

Because all the integrals of the Galerkin scheme are found analytically in terms of Bessel functions, calculations do not need numerical quadrature formulas. Results on the natural frequencies and modes are reported in Sections 4 and 5. The results depend on Sn, the number of screen gaps (slots, openings), the position of these gaps relative to the mean free surface, and the liquid depth. A comparison with experimental resonance frequencies from [8] performed with a small lateral forcing amplitude shows a satisfactory agreement with our theoretical natural sloshing frequencies unless the experimental studies report clearly nonlinear wave motions. The natural sloshing modes contain a term responsible for local inflow to the screen openings and terms describing a local flow at the edges within the framework of our hydrodynamic model. By the inflow is meant that we do not account for a local flow at the edges, i.e. we consider the dominant velocity field at a distance from the openings that is the order of the opening dimension. The inflow-related term can in future studies be used for more accurate prediction of the pressure jump at the screen caused by local flow by accounting for either flow separation or jet flow by, for instance, using empirically determined pressure loss coefficients [9]. Present state-of-the-art procedures neglect the influence of the screen on the inflow velocity [3,4].

2. Statement of the problem

2.1. Slat-type screen

We consider linear two-dimensional liquid sloshing in a rectangular tank with a slat-type screen installed at the tank middle as shown in Fig. 1. The screen appears as a thin solid plate with a series of perforated horizontal slots. Schematically, it is shown in Fig. 1a (see, also, Fig. 7 representing the screens of the experimental setup in [4,8]). The screen thickness is neglected.

In contrast to nets and wire-mesh screens [2,9], the slat-type screen geometry is characterized by a rather limited number of gaps, especially, for larger total solidity ratios. This number does not exceed 100 and, typically, is somewhere about 5–20. This means that the actual solidity ratio of the *wetted* screen part, Sn, depends on the liquid depth *h* and,
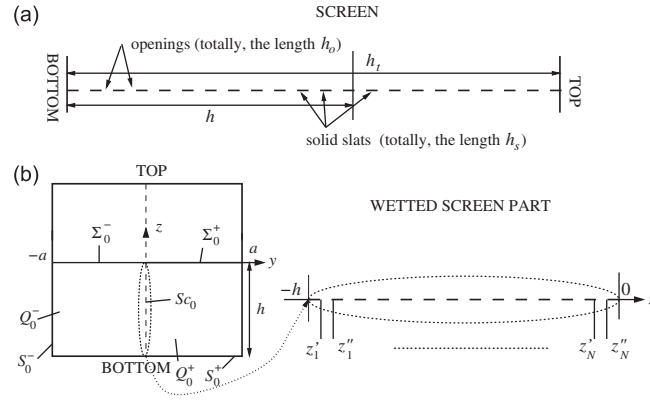
Fig. 1. Sketch of the screen-equipped rectangular tank.

generally, differs from the total solidity ratio $Sn_t = h_s/h_t = (h_t - h_o)/h_t$ (h_t is the total screen height, h_o is the total height of the perforation, and h_s is the total height of the rigid slats). Examples of these dependencies will be presented in Section 4.3.

In our analysis, we consider only the mean wetted screen part Sc_0 and assume that it has N submerged perforations defined by the numerical sequence $-h \leq z'_1 < z''_1 < z'_2 < z''_2 < \cdots < z'_N < z''_N \leq 0$ (see, Fig. 1b). When So_0 denotes all the wetted rigid slats, and Op_0 is the total set of submerged slots ($Sc_0 = Op_0 \cup So_0$), this numerical sequence defines

$$So_0 = \{(0,z) : -h \leq z \leq z'_1, z''_1 \leq z \leq z'_2, \ldots, z''_N \leq z \leq 0\},$$
$$Op_0 = \{(0,z) : -h \leq z'_1 < z < z''_1, \ldots, z'_N < z < z''_N \leq 0\}, \tag{1}$$

where h is the liquid depth.

Based on definition (1), we can introduce the solidity ratio of the mean wetted screen part as follows:

$$Sn = \frac{h - \sum_{j=1}^{N}(z''_j - z'_j)}{h}. \tag{2}$$

2.2. Spectral boundary problem

We consider a two-dimensional rectangular tank of the horizontal dimension $l = 2a$ equipped with a slat-type screen Sc_0 which divides the whole mean liquid domain Q_0 into two geometrically-equal rectangular compartments, Q_0^- and Q_0^+ (Fig. 1b). An ideal incompressible liquid with irrotational flow is assumed. Based on the corresponding linear sloshing theory (see, e.g. the books [2,10]), we will formulate a spectral boundary problem which describes natural (eigen) sloshing modes and frequencies. For this purpose, we introduce the natural sloshing frequency σ and the velocity potentials $\exp(i\sigma t)\varphi^+(y,z)$ and $\exp(i\sigma t)\varphi^-(y,z)$ ($i^2 = -1$) in Q_0^+ and Q_0^-, respectively. This spectral boundary problem is then formulated with respect to $\varphi^\pm$ (natural sloshing modes) and should include the Laplace equation, the zero-Neumann boundary condition on the wetted walls/bottom, and the spectral boundary condition on the mean free surface Σ_0 [2, Eq. (4.7)]

$$\frac{\partial^2 \varphi^\pm}{\partial y^2} + \frac{\partial^2 \varphi^\pm}{\partial z^2} = 0 \quad \text{in } Q_0^\pm, \tag{3a}$$

$$\frac{\partial \varphi^\pm}{\partial y} = 0 \quad \text{on } S_0^\pm, \tag{3b}$$

$$\frac{\partial \varphi^\pm}{\partial z} = \kappa\varphi \quad \text{on } \Sigma_0^\pm, \tag{3c}$$

where the spectral parameter κ determines the natural sloshing frequency

$$\sigma = \sqrt{g\kappa} \tag{4}$$

(g is the gravity acceleration).

Because of the screen, the problem requires transmission conditions on Sc_0 which should govern a 'no-cross-flow' condition at So_0, and continuity of $\varphi^\pm$ and $\partial\varphi^\pm/\partial y$ at the perforations Op_0, i.e.

$$\frac{\partial \varphi^\pm}{\partial y} = 0 \quad \text{on } So_0, \tag{5a}$$

$$\frac{\partial \varphi^+}{\partial y} = \frac{\partial \varphi^-}{\partial y} \quad \text{and} \quad \varphi^+ = \varphi^- \quad \text{on } Op_0, \tag{5b}$$

where So_0 and Op_0 are defined by Eq. (1).

When the tank has no screen, condition (5a) disappears, but transmission conditions (5b) become defined on $Op_0 = \{(0,z) : -h < z < 0\}$. The spectral boundary problem (3), (5b) has then the well-known nontrivial solution

$$\varphi_k^\pm = \phi_k = \cos\left(\frac{\pi k}{l}(y+a)\right)\cosh\left(\frac{\pi k}{l}(z+h)\right),$$

$$\kappa_k = \lambda_k = \frac{\pi k}{l}\tanh\left(\frac{\pi k h}{l}\right), \quad k = 1,\ldots \tag{6}$$

which defines the natural sloshing modes ϕ_k and frequencies by formula (4).

Analytical solution (6) for the clean rectangular tank contains the Oz-symmetric (even) natural modes ϕ_{2i}, and the Oz-antisymmetric (odd) modes ϕ_{2i-1}, $i=1,2,\ldots$. Because the symmetric modes satisfy the transmission conditions (5a), they *remain a solution* of the spectral boundary problem (3)–(5) when a slat-type screen in the middle of the tank is introduced. In contrast, the antisymmetric modes do not satisfy the Neumann transmission condition (5a).

The screen-modified antisymmetric modes have a jump at So_0, i.e. $\varphi^+ \neq \varphi^-$ on So_0, but they are continuous on Op_0. Because the continuous antisymmetric functions should be equal to zero at $y=0$, the Dirichlet transmission condition of (5b) can be replaced for the antisymmetric modes by the condition

$$\varphi^\pm = 0 \quad \text{on } Op_0. \tag{7}$$

2.3. An integral representation of the antisymmetric natural sloshing modes

For brevity of the forthcoming mathematical expressions, we consider the a-scaled problem (3)–(5) with $\overline{h} = h/a, \overline{\kappa} = a\kappa, \overline{z}'_j = z'_j/a, \overline{z}''_j = z''_j/a$ so that the horizontal dimension of compartments Q_0^+ and Q_0^- become 1. In addition, we omit superscript 'minus' for φ^- so that, by definition, $\varphi = \varphi^-$ in Q_0^-.

Let us assume that we know the normal velocity at each perforation given by functions $u_j(z)$, $j=1,\ldots,N$, i.e.

$$\left.\frac{\partial\varphi}{\partial y}\right|_{y=0} = u_j(z), \quad z'_j < z < z''_j, j = 1,\ldots,N, \tag{8}$$

and replace the Neumann transmission condition of (5b) by condition (8). Proceeding with the mixed boundary value problem (3), (5a) and (8) where $\overline{\kappa}$ is a constant value in the spirit of external surface wave problems (see, e.g. [5,7]), we arrive at the following integral representation:

$$\varphi(y,z) = \sum_{j=1}^{N}\int_{\overline{z}'_j}^{\overline{z}''_j} u_j(z_1)\mathcal{G}_{\overline{\kappa}}(y,z,z_1)\,dz_1, \tag{9}$$

where

$$\mathcal{G}_{\overline{\kappa}}(y,z,z_1) = -\frac{\cosh(k_0(z_1+\overline{h}))\cosh(k_0(z+\overline{h}))}{k_0 N_0}\frac{\cos(k_0(y+1))}{\sin(k_0)}$$

$$+ \sum_{i=1}^{\infty}\frac{\cos(k_i(z_1+\overline{h}))\cos(k_i(z+\overline{h}))}{k_i N_i}\frac{\cosh(k_i(y+1))}{\sinh(k_i)}. \tag{10}$$

Finally, because we look for antisymmetric modes,

$$\varphi^-(y,z) = \varphi(y,z) \text{ in } Q_0^- \quad \text{and} \quad \varphi^+(y,z) = -\varphi(-y,z) \text{ in } Q_0^+. \tag{11}$$

The integral kernel $\mathcal{G}_{\overline{\kappa}}$ is, in fact, a Green function constructed for the liquid domain Q_0^- which has been restricted to the boundary conditions on Σ_0^- and S_0^-. It depends on the nondimensional spectral parameter $\overline{\kappa}$. The reason is that k_i, N_i, $i=0,1,\ldots$, are roots of the transcendental equations

$$k_0\tanh(k_0\overline{h}) = \overline{\kappa}, \quad N_0 = \frac{1}{2}\overline{h}\left(1 + \frac{\sinh(2k_0\overline{h})}{2k_0\overline{h}}\right), \tag{12a}$$

$$k_i\tanh(k_i\overline{h}) = -\overline{\kappa}, \quad N_i = \frac{1}{2}\overline{h}\left(1 + \frac{\sin(2k_i\overline{h})}{2k_i\overline{h}}\right), \quad i = 1,2,\ldots \tag{12b}$$

which parametrically depend on $\overline{\kappa}$. To derive the Green function $\mathcal{G}_{\overline{\kappa}}$, we followed the analytical technique in [5,7] based on separation of spatial variables y and z in the mixed boundary value problem (3), (5a) and (8).

The Green function $\mathcal{G}_{\overline{\kappa}}$ is defined by the i-index functional series. Even though the series is numerically truncated, it *analytically* satisfies all the required boundary conditions except the boundary conditions on the screen. Moreover, this truncated series exponentially converges to the solution of (3), (5a) and (8) at each point of Q^- except on Sc_0. This is an advantage of using the integral representation (9).

Enforcing the zero-Dirichlet boundary condition (7) leads to the following system of homogeneous integral equations with respect to unknown functions $u_j(z)$, $j=1,\ldots,N$, and spectral parameter $\overline{\kappa}$

$$\sum_{j=1}^{N} \int_{\overline{z}'_j}^{\overline{z}''_j} u_j(z_1)\mathcal{G}_{\overline{\kappa}}(0,z,z_1)\,\mathrm{d}z_1 = 0, \quad \overline{z}'_k < z < \overline{z}''_k, \ k = 1,\ldots,N. \tag{13}$$

Now, the mathematical task consists of finding $\overline{\kappa}$, for which this homogeneous system has a nontrivial solution in terms of $u_j(z)$, $j=1,\ldots,N$. Substituting this nontrivial solution into representation (9) and Eq. (11) leads to the corresponding antisymmetric natural sloshing modes. An important practical matter is convergence in applying Eq. (13) and the output ($\overline{\kappa}$ and $u_j(z)$, $j=1,\ldots,N$) versus the truncated Green function representation and the input parameters, e.g. z'_j and z''_j. This convergence should become faster when the approximate solution $u_j(z)$, $j=1,\ldots,N$ accounts for the local flow singularities at the sharp edges. Such an approximate solution will be proposed in the next section. Furthermore, a special analytical technique will be applied in Appendix A which accelerates convergence in summation by i in the Green function representation.

3. Solving the integral equations (13)

3.1. Galerkin scheme

We present a nontrivial *approximate* solution of the homogeneous integral equation (13) in the form

$$u_j(z) = \sum_{l=1}^{M} b_{jl} f_{jl}(z), \quad \overline{z}'_j < z < \overline{z}''_j, \ j = 1,\ldots,N, \tag{14}$$

where $\{f_{jl}(z), l \geq 1\}$ is a complete set of trial functions on intervals $(\overline{z}'_j, \overline{z}''_j)$, $j=1,\ldots,N$, and $\{b_{kl}\}$ are unknown weight coefficients. A Galerkin variational scheme with increasing number M of coordinate functions on each gap is used to find these weight coefficients. According to this scheme, the approximate solution (14) should be substituted into Eq. (13), multiplied by $f_{kn}(z)$ on the corresponding intervals $(\overline{z}'_k, \overline{z}''_k)$, and integrated over this interval. Proceeding this way yields the homogeneous system of linear algebraic equations with respect to the $(M \cdot N)$ weight coefficients $\{b_{jl}, j=1,\ldots,N; l=1,\ldots,M\}$

$$\sum_{j=1}^{N} \sum_{l=1}^{M} B_{kn,jl}^{\overline{\kappa}} b_{jl} = 0, \tag{15}$$

where the symmetric matrix elements $B_{kn,jl}^{\overline{\kappa}}$ take the form

$$B_{kn,jl}^{\overline{\kappa}} = \int_{\overline{z}'_j}^{\overline{z}''_j} \int_{\overline{z}'_k}^{\overline{z}''_k} f_{kn}(z)\mathcal{G}_{\overline{\kappa}}(0,z,z_1)f_{jl}(z_1)\,\mathrm{d}z\,\mathrm{d}z_1$$

$$= -\frac{c_{kn}^{(0)} c_{jl}^{(0)}}{\tan(k_0)k_0 N_0} + \sum_{i=1}^{\infty} \frac{c_{kn}^{(i)} c_{jl}^{(i)}}{\tanh(k_i)k_i N_i}. \tag{16}$$

Here, we have introduced the notations

$$c_{pq}^{(0)} = \int_{\overline{z}'_p}^{\overline{z}''_p} f_{pq}(z)\cosh(k_0(z+\overline{h}))\,\mathrm{d}z, \quad c_{pq}^{(i)} = \int_{\overline{z}'_p}^{\overline{z}''_p} f_{pq}(z)\cos(k_i(z+\overline{h}))\,\mathrm{d}z, \ i \geq 1. \tag{17}$$

A nontrivial solution of the homogeneous system (15) is only possible if the determinant of the $(NM) \times (NM)$ matrix $\|B_{kn,jl}^{\overline{\kappa}}\|$ is zero, i.e.

$$\det\|B_{kn,jl}^{\overline{\kappa}}\| = 0. \tag{18}$$

Eq. (18) should be considered as a transcendental equation with respect to nondimensional spectral parameter $\overline{\kappa}$. Each [enumerated] root $\overline{\kappa}_m$ of this transcendental equation (18) is, in fact, an approximate nondimensional eigenvalue for the corresponding antisymmetric natural mode. To find this natural mode in an analytical form, we should solve the homogeneous matrix problem

$$\|B_{kn,jl}^{\overline{\kappa}_m}\|\{b_{jl}\} = 0, \tag{19}$$

substitute the nontrivial solution vector $\{b_{jl}\}$ into (14) and, thereafter, in representation (9). Going this way, we get

$$\varphi(y,z) = -\frac{\cosh(k_0(z+\overline{h}))\cos(k_0(y+1))}{k_0 N_0 \sin(k_0)}A_0 + \sum_{i=1}^{\infty} \frac{\cos(k_i(z+\overline{h}))\cosh(k_i(y+1))}{k_i N_i \sinh(k_i)}A_i, \tag{20}$$

where

$$A_i = \sum_{l=1}^{M} \sum_{j=1}^{N} b_{jl} c_{jl}^{(i)}, \quad i = 0, 1, \dots . \tag{21}$$

3.2. Coordinate functions $\{f_{kl}(z)\}$

To get an accurate Galerkin approximation, the chosen coordinate functions $\{f_{kl}(z)\}$ should capture local asymptotics of $u_j(z)$ at the sharp edges, namely, at the points z'_j and z''_j. This local asymptotics should be the same as for a steady irrotational flow of an ideal incompressible liquid through an orifice plate (see, e.g. [11]). In the notations of Fig. 2 for the local flow plane (τ_1, τ_2), the normal velocity $u(\tau_1)$ is characterized by the local asymptotics

$$C_\pm (\tau_1 \pm 1)^{[q-1]-1/2}, \quad q = 1, \dots, \text{ as } \tau_1 \to \pm 1. \tag{22}$$

One must note that our problem requires consideration of a cross-flow with $C_- \neq C_+$ in Eq. (22). The reason is an exponential decay of the natural sloshing modes along the screen causing different local velocities at z'_j and z''_j of the same gap (Fig. 2). To match this nonsymmetric flow in the local plane, we can introduce symmetric and antisymmetric (with respect to $O\tau_2$) trial functions

$$g_q^{(1)}(\tau_1) = (1 - \tau_1^2)^{[q-1]-1/2}, \quad \text{and} \quad g_q^{(2)}(\tau_1) = \tau_1(1 - \tau_1^2)^{[q-1]-1/2}, \; q \geq 1. \tag{23}$$

Whereas $q=1$, these functions capture the main singularity at $\tau_1 = \pm 1$ with different weight coefficients C_+ and C_- provided by a linear combination of $g^{(1)}(\tau_1)$ and $g^{(2)}(\tau_1)$. The regular (continuous) velocity field component can be approximated by the continuous functional set $\{g_q^{(1)}(\tau_1), g_q^{(2)}(\tau_1), q \geq 2\}$ which is complete due to Müntz' theorem [12].

Employing the functional basis (23) in the original plane $(p=1, \dots, N; M = L_1 + L_2)$ implies

$$f_{pq}(z) = g_q^{(1)}\left(-1 + \frac{2}{\overline{z}''_p - \overline{z}'_p}(z - \overline{z}'_p)\right), \quad q = 1, \dots, L_1,$$
$$f_{p(q+L-1)} = g_q^{(2)}\left(-1 + \frac{2}{\overline{z}''_p - \overline{z}'_p}(z - \overline{z}'_p)\right), \quad q = 1, \dots, L_2. \tag{24}$$

An advantage of the coordinate functions (24) is that they make it possible to get *exact analytical expressions* for quadratures $c_{pq}^{(0)}$ and $c_{pq}^{(i)}$ by using Poisson's integrals [13, Section 3.3]. These expressions are

$$c_{pq}^{(0)} = \sqrt{\pi}[\Delta'_p \cosh \beta_0^{(p)}][2^{q-2} \Gamma(q - \tfrac{1}{2})][(\alpha_0^{(p)})^{1-q} I_{q-1}(\alpha_0^{(p)})], \tag{25a}$$

$$c_{p(L-1+q)}^{(0)} = \sqrt{\pi}[\Delta'_p \sinh \beta_0^{(p)}][2^{q-2} \Gamma(q - \tfrac{1}{2})][(\alpha_0^{(p)})^{1-q} I_q(\alpha_0^{(p)})], \tag{25b}$$

$$c_{pq}^{(i)} = \sqrt{\pi}[\Delta'_p \cos \beta_i^{(p)}][2^{q-2} \Gamma(q - \tfrac{1}{2})][(\alpha_i^{(p)})^{1-q} J_{q-1}(\alpha_i^{(p)})], \tag{25c}$$

$$c_{p(L-1+q)}^{(i)} = -\sqrt{\pi}[\Delta'_p \sin \beta_i^{(p)}][2^{q-2} \Gamma(q - \tfrac{1}{2})][(\alpha_i^{(p)})^{1-q} J_q(\alpha_i^{(p)})], \tag{25d}$$

where

$$\Delta'_p = \overline{z}''_p - \overline{z}'_p, \quad \alpha_i^{(p)} = \tfrac{1}{2} k_i \Delta'_p, \quad \beta_i^{(p)} = k_i(\overline{h} + z_p^*), \quad z_p^* = \tfrac{1}{2}(\overline{z}''_p + \overline{z}'_p), \tag{26}$$
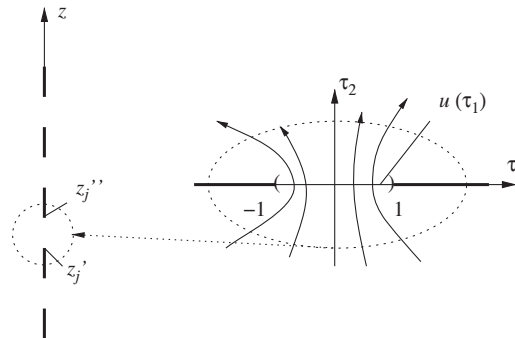

Fig. 2. Sketch of a local instantaneous flow through an single gap in the local (τ_1, τ_2)-plane. We define $u(\tau_1) = \partial \phi / \partial \tau_2|_{\tau_2 = 0}$, where $\phi(\tau_1, \tau_2)$ is the local velocity potential in the (τ_1, τ_2)-plane.

$\Gamma(\cdot)$ is the Gamma-function, and $J_p(\cdot)$ and $I_p(\cdot)$ are the Bessel functions of the first kind, and the modified Bessel function of the first kind, respectively.

Expressions (25) should be substituted into Eq. (16) to compute the symmetric matrix $\|B_{kn,jl}^{\overline{\kappa}}\|$. The procedure needs a numerical summation of the series by index i. Accounting for the limits

$$\kappa_i \approx \frac{\pi i}{h}, \ i \to \infty, \quad J_\alpha(x) \approx \sqrt{\frac{2}{\pi x}}\cos\left(x - \frac{1}{2}\alpha\pi - \frac{1}{4}\pi\right), \ x \to \infty, \tag{27}$$

we can show that these numerical series converge absolutely.

Summation of the numerical series in Eq. (16) deals, except for $B_{k\ 1,j\ 1}$, $B_{k(L_1+1),j1}$, $B_{k1,j(L_1+1)}$, and $B_{k(L_1+1),j(L_1+1)}$, with the $O(1/i^3)$- and $o(1/i^3)$-order terms. This means that, if we take K elements of these numerical series, the convergence error is of the order $O(1/K^2)$ and $o(1/K^2)$, respectively, which is, generally, satisfactory for our FORTRAN code providing 10–12 significant figures with K=100 000. A slower convergence is expected for $B_{k\ 1,j\ 1}$, $B_{k(L_1+1),j1}$, $B_{k1,j(L_1+1)}$, and $B_{k(L_1+1),j(L_1+1)}$, whose numerical computation involves the $O(1/i^2)$-order terms. However, the latter convergence can be improved to have the $O(1/K^2)$-order error by employing the analytical results in Appendix A.

4. Natural frequencies

4.1. A single gap

When the considered screen has a single gap (N=1 in Eq. (1)), Eq. (2) transforms to

$$1 - \frac{\overline{z}''_1 - \overline{z}'_1}{h} = \text{Sn}. \tag{28}$$

Eq. (28) couples the end coordinates of this single gap, the liquid depth, and the solidity ratio.

4.1.1. Baffle

When varying the coordinate $\overline{z}''_1$ with $\overline{z}'_1 = -\overline{h}$, we arrive at the free-surface piercing baffle. The case of $\overline{z}''_1 = 0$ with the varied coordinate $\overline{z}'_1$ corresponds to the bottom-mounted baffle. The numerical eigenvalues $\overline{\kappa}_i$, $i = 1,3,5$, for these two limit 'baffle' problems are presented in [14,15]. Fig. 3 shows that our approximate solution is in a good agreement with these values.

When computing the eigenvalues in Fig. 3, we establish a rather fast numerical convergence. Using $L_1=L_2=8$, $M=L_1+L_2=10$ in Galerkin' solution (14) with coordinate functions (24) provides 6–7 stabilized significant figures of $\overline{\kappa}_1,\overline{\kappa}_3$ and $\overline{\kappa}_5$ for all the baffle sizes l_b. Moreover, when the gap size is smaller, $(1-l_b/h) \lesssim 0.15$, six significant figures of these three nondimensional eigenvalues are stabilized with $L_1=L_2=2$. The reason for this fast convergence is that our coordinate functions account for the singular behavior of the velocity field at the sharp edges. These singularities provide dominant contribution to the original solution, especially, for smaller gap sizes.

Fig. 3 presents the nondimensional eigenvalues $\overline{\kappa}_i, i = 1,3,5$, versus Sn$=l_b/h$ with h/l=1. The dashed lines denote the surface-piercing baffle case, but the solid lines give the numerical eigenvalues for the bottom-mounted baffle case. As we have remarked in Section 2.2, the symmetric modes remain the same as for the clean tank; these are defined by Eq. (6).
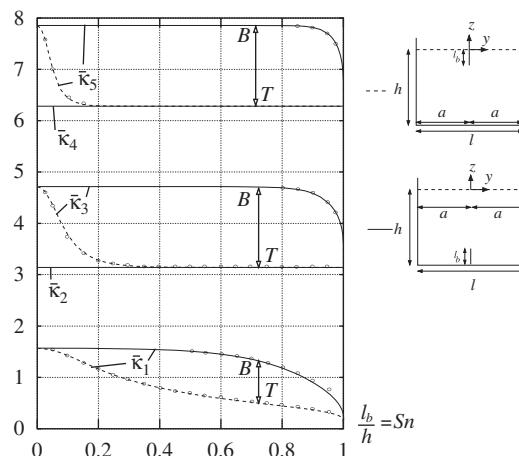

Fig. 3. The nondimensional eigenvalues $\overline{\kappa}_n = \frac{1}{2}\kappa_n l = \kappa_n a$, $n = 1,\ldots,5$, versus the nondimensional baffle size l_b/h with h/l=1. The ratio l_b/h is the same as the solidity ratio Sn for the studied case. The dashed lines show results for the surface piercing baffle, but the solid lines denote calculations done for the bottom-mounted baffle. The numerical results are compared with those in [14,15] (circles).

The corresponding nondimensional eigenvalues for the two lowest symmetric modes are denoted by $\overline{\kappa}_2$ and $\overline{\kappa}_4$. Asymptotic limits of $\overline{\kappa}_1, \overline{\kappa}_3$ and $\overline{\kappa}_5$ are discussed in [14] and we refer interested readers to this paper for more details.

Some interesting comments can be added for the case Sn→1. For the lowest eigenvalue $\overline{\kappa}_1$ of the surface-piercing baffle problem, when the baffle edge approaches the bottom, there is a similarity with the U-tube problem. Our calculations show a stabilization of the $\overline{\kappa}_1$−value when Sn numerically tends to 1. However, when $0.99999 < \text{Sn} < 1$, i.e. until the tank which is almost fully divided by the baffle, this eigenvalue as well as the eigenvalues for the bottom-mounted baffle rapidly drop to zero and the eigenvalues $\overline{\kappa}_2$ and $\overline{\kappa}_4$, respectively. The same 'drop' was reported in [14] with a reference to Tuck [16] who considered the effect of a submerged barrier on the natural sloshing frequencies of a basin connected with an open water. We can also refer to the book [2, pp. 167–168] in which such a rapid change is reported for the added mass coefficient of two plates in a side-by-side arrangement in an infinite fluid when the two plates are close and approaching each other.

An important property is that the surface-piercing baffle leads to a faster decrease of the eigenvalues relative to that for the bottom-mounted baffle. This can be seen by comparing two values at points B and T corresponding to the same input Sn. The bigger difference at these points is in the range $0.2 \lesssim \text{Sn} \lesssim 0.8$ when the surface-piercing baffle reduces $\overline{\kappa}_3$ and $\overline{\kappa}_5$ to $\overline{\kappa}_2$ and $\overline{\kappa}_4$, respectively, but the bottom-mounted baffle leads to almost zero effect. This fact is explained by an exponential decay of the natural sloshing modes to the bottom. Being situated far from the mean free surface where a 'mainstream' occurs, the bottom-mounted baffle cannot influence the liquid flux between Q_0^+ and Q_0^-, but the surface-piercing baffle can do it.

4.1.2. A single gap between the mean free surface and the bottom

We consider the case $-h < z'_1 < z''_1 < 0$, which means that there are surface-piercing and bottom-mounted baffles, simultaneously. For a constant solidity ratio Sn in relation (28), we get the restriction

$$-1 + \tfrac{1}{2}(1-\text{Sn}) < z_1^*/h = \overline{z}_1^*/\overline{h} < -\tfrac{1}{2}(1-\text{Sn}) \tag{29}$$

for the middle point z_1^* of the single screen gap defined in Eq. (26).

The solid lines in Fig. 4 show changing $\overline{\kappa}_1$ and $\overline{\kappa}_3$ versus z_1^*/h in the interval (29). The points B ($z_1^*/h = -\tfrac{1}{2}(1-\text{Sn})$) and T ($z_1^*/h = -1 + \tfrac{1}{2}(1-\text{Sn})$) denote the two limit cases (scenarios) when z_1^*/h equals to the ends of this interval and, thereby, the screen becomes bottom-mounted and surface-piercing baffle, respectively. The dashed lines are used to show what happens with the considered eigenvalues when z_1^*/h moves outside of interval (29) with appropriate increase of the solidity ratio.

By analyzing the solid lines in Fig. 4 for different constantly fixed solidity ratio, we observe the following. For smaller solidity ratios, $\text{Sn} \lesssim 0.5$, the solid lines illustrate monotonically increasing functions of z_1^*/h whose absolute maximum occurs at the end B, i.e. when the screen becomes a bottom-mounted baffle without intersection of the mean free surface. This fact looks quite logical, if we deal with results in Fig. 3 where there are two limit positions, T and B. Varying the gap position between these limit points monotonically changes the eigenvalues, so that a minimum modification of the eigenvalues due to the screen (κ_1^* and κ_3^* denote the nondimensional eigenvalues for the clean tank) is for the limit case B (bottom-mounted baffle).

However, the solid lines in Fig. 4 are not monotonic functions of z_1^*/h for larger solidity ratios, $0.5 \lesssim \text{Sn}$. The minimum difference between κ_i^* and $\overline{\kappa}_i, i = 1,3$, is found slightly left of the point B. At these extrema points, the screen consists of a long bottom-mounted baffle and a small surface-piercing baffle, simultaneously. Occurrence of such an 'optimum' position of the screen gap which differs from position B can be explained in the following way.

First of all, we remark that, according to asymptotic estimates in [15] (see, also, [2, Chapter 4]), a small surface-piercing baffle of nondimensional length δ provides an $O(\delta^2)$-decrease of the eigenvalues. Furthermore, we should look at the solid lines in Fig. 3 to realize what is the effect of a δ−length variation of the long bottom-mounted baffle. We see that when $\text{Sn} \lesssim 0.5$ (for $\overline{\kappa}_1$) and $\text{Sn} \lesssim 0.8$ (for $\overline{\kappa}_3$ and $\overline{\kappa}_5$), these solid lines are almost horizontal. This means that there is no clear $O(\delta)$- or $O(\delta^2)$−contribution into the eigenvalues due to a δ−length variation of the bottom-mounted baffle. The eigenvalues are, therefore, effected only by the small-piercing baffle. The latter conclusion leads to a local maximum at B for smaller Sn due to the aforementioned asymptotic results in [15]. However, when $0.5 \lesssim \text{Sn}$ for $\overline{\kappa}_1$ and $0.8 \lesssim \text{Sn}$ for $\overline{\kappa}_3$ and $\overline{\kappa}_5$, the tangent to the solid lines in Fig. 3 is not horizontal so that a δ−length variation of the long bottom-mounted baffle includes a linear, $O(\delta)$−order contribution to the eigenvalues. This means that a small variation of the long bottom-mounted baffle provides a leading-order change of the eigenvalues and the $O(\delta^2)$−variations due to a small surface-piercing baffle can be neglected in the first-order approximation. As a consequence for the larger solidity ratios, because the derivatives of the solid-line graphs in Fig. 3 are negative, the solid-line graphs in Fig. 4 should also have a negative derivative at B. The local maximum at B becomes then impossible.

4.2. Eigenvalues as functions of Sn, N, and the position of the perforations

When we have many submerged perforations (gaps), the eigenvalues become complicated functions of the solidity ratio, the number of gaps N, and, as we showed in Section 4.1.2, the position of gaps with respect to the mean free surface. To illustrate such a dependence, we keep a constant liquid depth (in our example, $h/l = 1$) and the h-scaled perforation
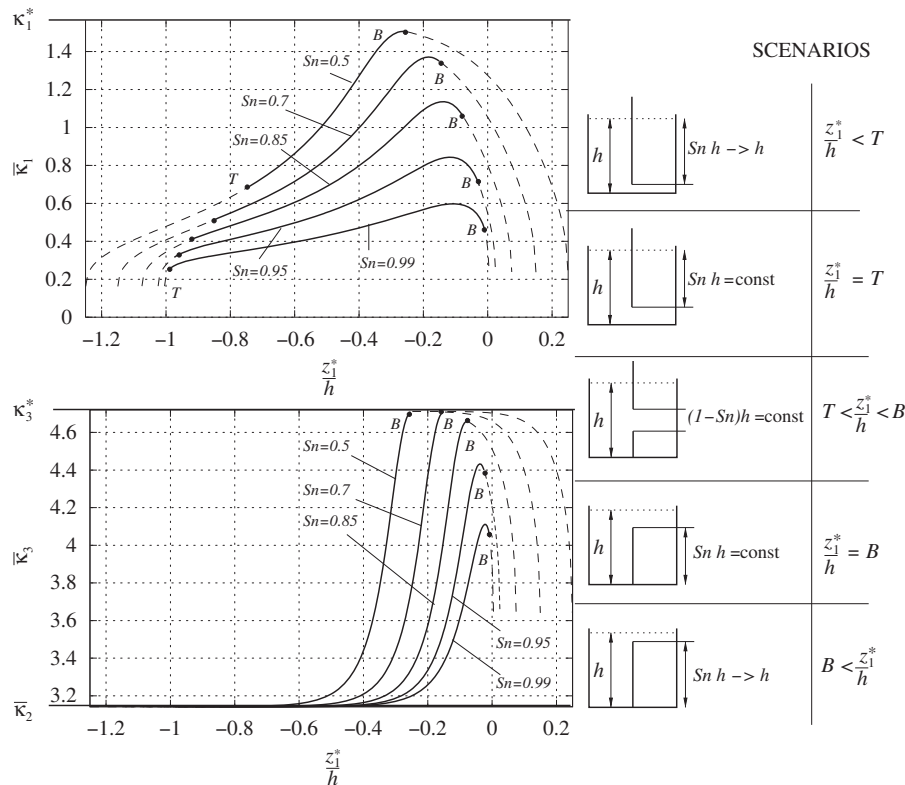
Fig. 4. The nondimensional eigenvalues $\overline{\kappa}_n = \frac{1}{2}\kappa_n l = \kappa_n a$, $n=1,3$, versus the nondimensional position of the single opening, $z_1^*/h = \frac{1}{2}(z_1' + z'' - 1)/h$, for different solidity ratios (solid lines). Scenario $z_1^*/h = T$ (point T) means that the screen becomes a surface-piercing baffle with the same constant value of Sn. Scenario $z_1^*/h < T$ (dashed lines in the left of T) implies decreasing Sn of this surface-piercing baffle. Scenario $z_1^*/h = B$ (point B) means that the screen becomes a bottom-mounted baffle with the same constant value of Sn. Scenario $B < z_1^*/h$ (dashed lines in the right of B) implies decreasing Sn of this bottom-mounted baffle. The depth-to-tank-breadth ratio h/l is 1. The values κ_1^* and κ_3^* denote the nondimensional eigenvalues for the clean tank, namely, $\kappa_i^* = \frac{1}{2}\lambda_i l, i = 1,2,3$, where λ_i is defined by Eq. (6).

height ($x_0 = 0.0075$), but vary the length between the slots whose h-scaled value is denoted by x. The nondimensional value x is the same as the h-scaled vertical dimension of the solid screen components. An explanation of this scenario is given in Fig. 5 (in the left top).

Fig. 5 presents dependencies of N, Sn and $\overline{\kappa}_i, i = 1,3,5$, on the h-scaled length between the openings, x. As long as N perforations are *completely* submerged into the mean liquid domain so that the upper opening is not intersected by the mean free surface, changing x does not effect the solidity ratio which remains a constant value. This fact follows from formula (2) giving $Sn = 1 - Nx_0 = const$ with constant values of N and x_0. It is also clearly seen in Fig. 5 by the graphs for N and Sn. The solid lines are used to mark this case in other panels. Let us analyze what happens with the eigenvalues with constant Sn and N, but a varied x-value.

Even though Sn and N remain constant values on the corresponding intervals of x, the solid lines in the graphs for $\overline{\kappa}_1, \overline{\kappa}_3$ and $\overline{\kappa}_5$ demonstrate a change for larger solidity ratios, $0.55 \lesssim Sn$. The shapes of the solid-line pieces $(D \to C)$ look similar to those in Fig. 4 where we have had the constant $N=1$ and Sn, but the single opening position has been varied with respect to the mean free surface. Again, we see local peaks on these solid lines when the upper submerged opening approaches the mean free surface. These peaks indicate a local minimum difference between the natural frequencies with the screen and the corresponding natural frequencies of the clean tank. The picture looks like there is an 'optimum' position of the uniformly perforated screen slots for which a minimum modification of the natural sloshing frequencies occurs with the same N and Sn. Furthermore, when the upper screen hole becomes intersected by the mean free surface (dashed lines) with an appropriate increase of the solidity ratio, the eigenvalues rapidly decrease to a local minimum value.

4.3. Eigenvalues as a function of h

The natural sloshing frequencies depend on the liquid depth. For the clean rectangular tank, this dependence is governed by Eq. (6). Slat-type screens lead to a difference from this dependence. An illustration of the fact is given in Fig. 6 for the four screens in Fig. 7 and rectangular tank of the breadth equal to 1 m.
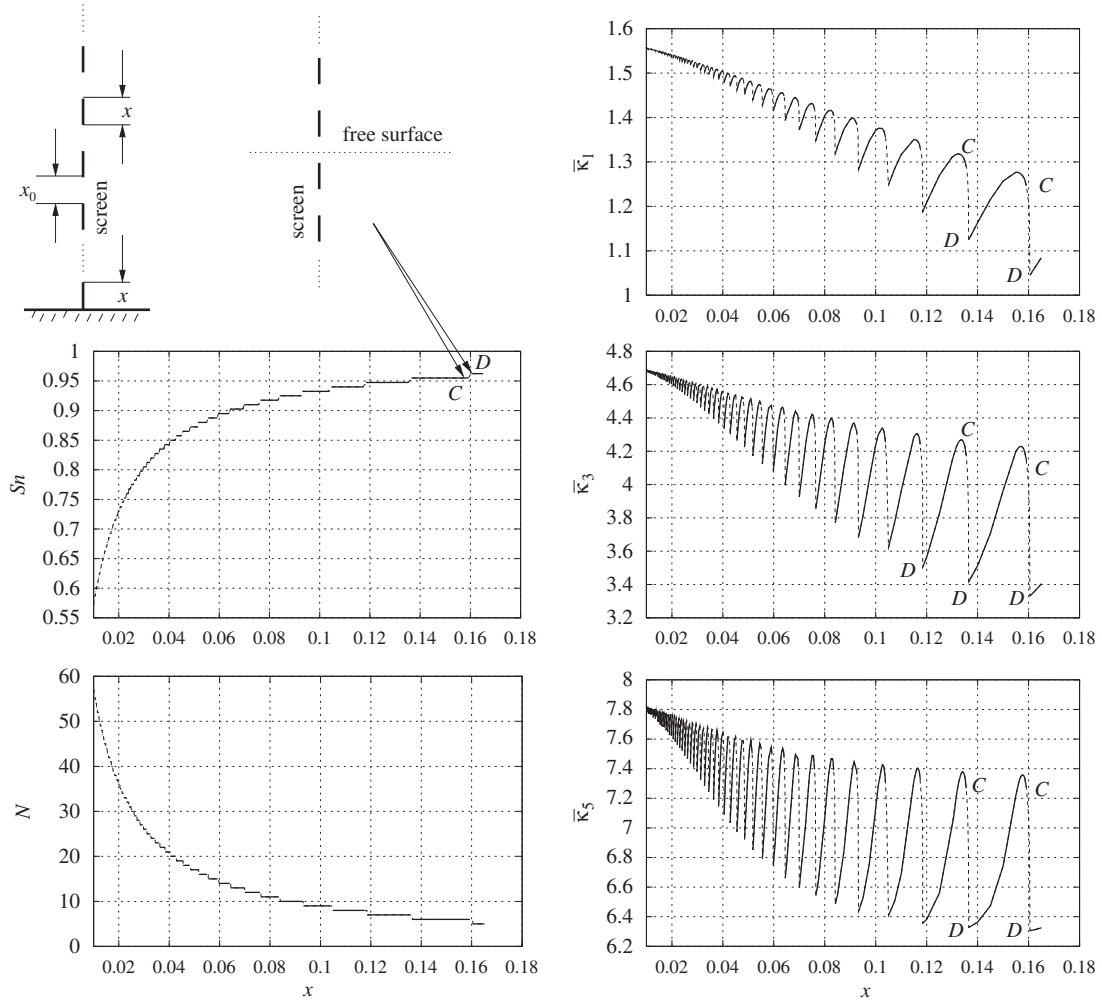
Fig. 5. The nondimensional eigenvalues $\overline{\kappa}_n = \frac{1}{2}\kappa_n l = \kappa_n a$, $n = 1,3,5$, the solidity ratio Sn, and the number of fully or partly submerged perforations (gaps) versus the distance between two nearest fully submerged gaps $x = (z'_{i+1} - z'_i)/h, i < N$ with $h/l = 1$. The h-scaled gap height $x_0 = (z''_i - z'_i)/h, i < N$ of the fully submerged perforations is assumed to be a constant value ($x_0 = 0.0075$ in calculations). As long as N perforations are fully submerged into the mean liquid domain, Sn remains a constant value (solid lines in all the panels). However, the upper screen opening can be intersected by the mean free surface which causes changing Sn (dashed lines between C and D).

First of all, we note that Sn is not a constant value, but an 'oscillatory' function of h/l. Fig. 6(a) shows that Sn increases with h/l on the intervals $(D \rightarrow C)$ where a solid screen part intersects the mean free surface, and Sn decreases with increasing h/l on the intervals $(C \rightarrow D)$ where the mean free-surface runs through a screen perforation. Variations of Sn are of maximum magnitude for smaller liquid depths when there is a few fully submerged screen slots. However, Sn stabilizes at an approximately constant value for larger values of h/l.

Furthermore, Fig. 6(b–d) shows that $\overline{\kappa}_1, \overline{\kappa}_3$, and $\overline{\kappa}_5$ (scaled by the corresponding eigenvalues for the clean tank) are very sensitive to variations of the solidity ratio for both smaller and larger liquid depth. This is even though Sn becomes an approximately constant value detected for larger h/l. A reason is that these eigenvalues may also be affected by positions of the screen openings which vary together with Sn in our numerical scenario. Because Sn is not a constant value, it is very difficult to distinguish which from these two factors (variation of Sn or positions of the openings) gives dominant contribution to the established 'oscillatory' change of the eigenvalues.

4.4. Comparison with experiments

Studies in [4,8] report experimental investigations of the resonant sloshing in a rectangular tank with a slat-type screen in the middle. The resonant sloshing occurred due to the horizontal harmonic forcing. Strongly damped and nonlinear resonant wave phenomena were observed. However, the experimental resonance frequency ranges evaluated with the lowest forcing amplitude can, under certain assumptions, be associated with the linear natural sloshing frequencies. These
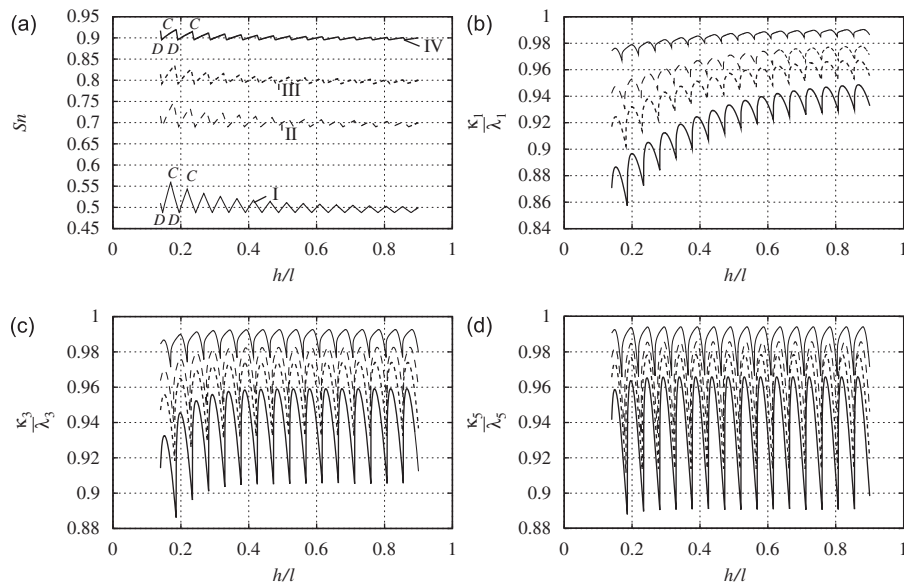
Fig. 6. Variation of the solidity ratio (a), and the ratios $\kappa_i/\lambda_i, i = 1,3,5$ (between the eigenvalues for the screen-equipped tank and the corresponding clean tank) in panels (b–d). The results are presented as functions of h/l. Calculations are done for the four screens in Fig. 7 and rectangular tank with the breadth of 1 m.
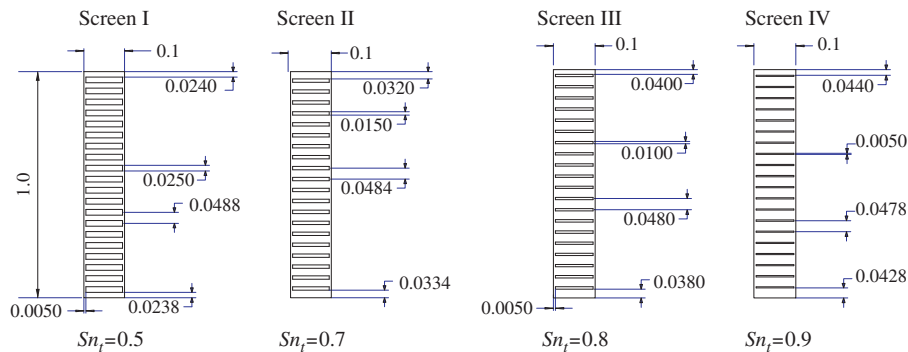

Fig. 7. Screens reported in experimental studies [4]. All the dimensions are in meters.

experimental ranges [8, Table 3] correspond to the forcing frequencies where the free-surface elevations demonstrate a local peak response. The experimental liquid depth-to-the-tank-breadth was h/l=0.4, the nondimensional forcing amplitude η_{2a}/l was about 0.001. For this depth and nine different screens, the experiments deal with Sn in the range $0.3 \leq Sn \leq 0.96$, the corresponding number of the submerged openings was $8 \geq N \geq 2$. Four screens from these experiments are shown in Fig. 7. The interested readers may find details on other screens in [4,8].

A comparison of the experimental *resonance* frequencies and our theoretical *natural* frequencies is presented in Fig. 8. The values $\overline{\sigma}_i = \sigma_i/\sigma_1^{Sn = 0}$ denote the ratios between the corresponding resonance/natural frequency and the lowest natural frequency for the clean tank. In notation of the present paper, according to formulas (4) and (6), $\overline{\sigma}_i = \sqrt{\kappa_i/\lambda_1}$. The triangles mark bounds of the experimental resonant frequency ranges, but the theoretical natural frequencies (scaled by the lowest natural sloshing frequencies of the clean tank) are connected by the solid lines.

Even though the linear theory is limited in predicting the resonance frequencies when the nonlinearity matters, we see a satisfactory agreement between the experimental frequency ranges and our theoretical values. The difference, we believe, is due to neglecting the pressure loss caused by flow separation or jet flow at the screen as well as the free-surface nonlinearity. The most visible difference is for $\overline{\sigma}_1$ with $Sn \geq 0.85$ when the experiments were not able to detect a clear resonant peak associated with the lowest natural sloshing mode. As discussed in [4], the reason is a strong nonlinear pressure loss due to flow separation or jet flow. The four experimental measurements with $Sn \geq 0.85$ detect a resonance response for the third mode. Two of these four experimental frequency ranges are in good agreement with our linear theory. However, there is a sufficient discrepancy for the remaining two experimental cases with $Sn \geq 0.946$ when the experiments report strongly nonlinear surface waves. For these two cases, an explanation comes from considering the 'soft-spring' behavior of the corresponding nonlinear response curves [4,8].
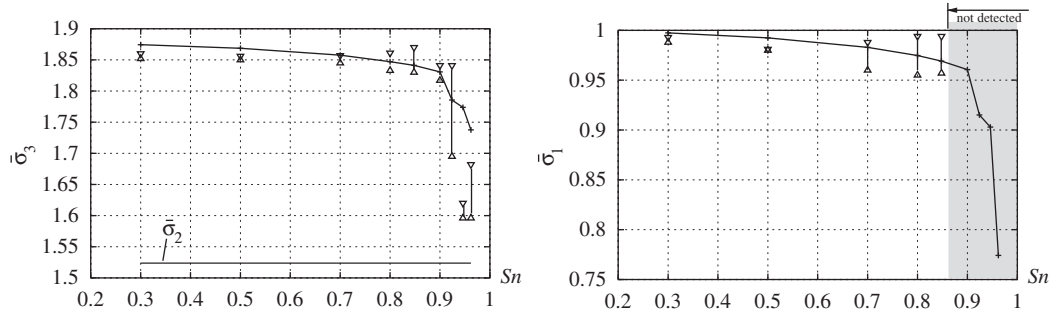
Fig. 8. The theoretical natural sloshing frequencies (cross-and-solid-line) and the ranges of the experimental resonant frequencies from [8, Table 3] (triangles). The values $\overline{\sigma}_i = \sigma_i/\sigma_1^{Sn=0}$ are the ratios between the corresponding resonance/natural frequency and the lowest natural sloshing frequency for the clean tank. In notations of the present paper, $\overline{\sigma}_i = \sqrt{\kappa_i/\lambda_1}$. The depth-to-tank-breadth ratio is $h/l=0.4$. The experiments were performed with the horizontal forcing of the nondimensional amplitude $\eta_{2a}/l = 0.001$. The experimental setup employed nine different screens (see [8,4] for more details); four of them are presented in Fig. 7. The shadow zone demonstrates the frequency range where the experiments were not able to detect a clear resonance peak due to a strong damping.
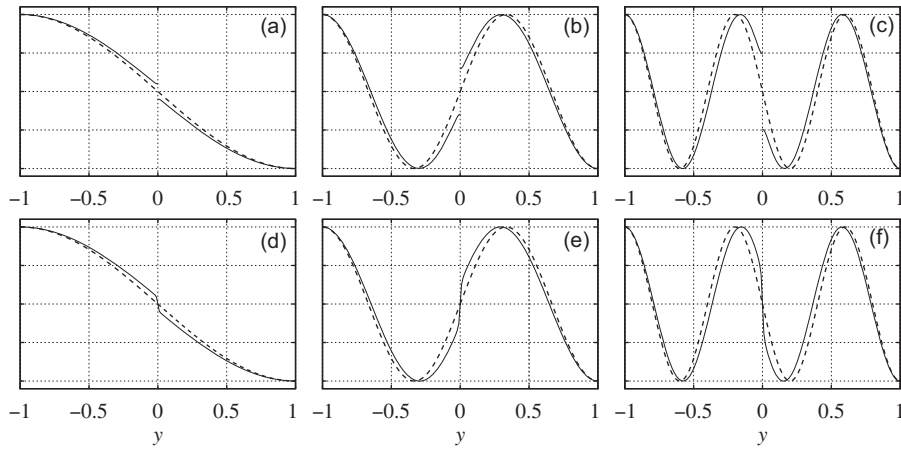

Fig. 9. The first three antisymmetric free-surface profiles associated with $\overline{\kappa}_1$ (a,d), $\overline{\kappa}_3$ (b,e), and $\overline{\kappa}_5$ (c,f). The tank breadth is 1 m, the screen IV in Fig. 7 is installed. The panels (a–c) display the free-surface profiles for $h/l=0.4$ when the mean free surface is separated by a solid piece of the screen. The panels (d–f) ($h/l=0.426$) are related to the case when the mean free surface is free going through the upper screen opening.

5. On the natural sloshing modes

Our calculations on the natural sloshing modes showed that the first term in expression (20) with coefficient A_0 gives a clearly dominant contribution to the natural sloshing modes for all the tested screens, Sn, N, and h. This is similar to 'one-term approximation' in [14] for a single baffle. Remaining terms are only important in a local neighborhood of the screen. They exponentially decay away from Sc_0 and, therefore, play only the role in providing an accurate satisfaction of the transmission conditions. However, these terms cannot be neglected in calculation of the eigenvalues. This becomes understandable from results of previous sections establishing that the eigenvalues undergo a change due to small local variation of the screen perforation. Based on only the A_0-dominant term, we are not able to show the strong parameter dependency of the eigenvalues.

Besides, keeping only the A_0-associated term leads always to a jump of the velocity potential (natural mode) at Sc_0. However, this jump should not be theoretically present within the framework of our hydrodynamic model when a solid screen part does not intersect the mean free surface. The $\{A_i, i \geq 1\}$–terms in (20) make it possible to capture the local asymptotics of the surface-wave profiles at the screen. This fact is illustrated in Fig. 9 by considering the three lowest antisymmetric modes in a rectangular tank with screen IV in Fig. 7 for two control liquid depths. In the case with $h/l=0.4$ (panels a–c), the mean free surface crosses a solid screen piece. The graphs show then a clear jump at $y=0$ which becomes larger for higher modes. However, the nondimensional depth $h/l=0.426$ corresponds to situation when the mean free surface goes though the upper screen perforation. In this case, the free surface profiles are continuous.

6. Conclusions

Using a domain decomposition method, we constructed an approximate solution for antisymmetric natural sloshing modes in a rectangular tank with a slat-type screen at the tank middle. The solution employs special coordinate functions

which capture the local asymptotics at the sharp edges of the slats. This provides an accurate approximation of the natural frequencies and modes so that 4–16 coordinate functions guarantee 6–7 significant figures of the three lowest eigenvalues for all the tested geometric configurations. A comparison with results in [14,15] is made for the case when the screen has a single gap located at either the bottom or the mean free surface, namely, for sloshing with a surface-piercing or bottom-mounted baffle. Very good agreement is documented.

When the single gap is not at either the bottom or the free surface, the result will depend on the position of this gap and Sn. For smaller solidity ratios, the minimum modification of the natural sloshing frequencies relative to those in the clean tank is found for the case when the screen becomes the bottom-mounted baffle. However, larger solidity ratios give this minimum for a single gap screen situated beneath the mean free surface so that the mean free surface is pierced by a small solid screen part.

Increasing number of the screen perforations shows that the natural sloshing frequencies (eigenvalues of the considered spectral problem) are complicated functions of the liquid depth, Sn, the number of the submerged perforations, and the position of these perforations. Based only on Sn, we cannot precisely predict these eigenvalues. When $0.5 \lesssim$ Sn with constant values of Sn and N, we demonstrate in Section 4.2 that the eigenvalues can vary with a nonnegligible magnitude due to varying position of the screen slots relative to the mean free surface. These variations become larger for larger Sn. The position of the gaps may, we believe, matter for an accurate calculation of the natural sloshing frequencies with different tank fillings.

A comparison with experimental data on the resonant sloshing frequencies taken from [8] for sufficiently small excitation amplitude shows satisfactory agreement with our theoretical natural sloshing frequencies. The differences can be explained by the nonlinearity caused by flow separation/jet flow, and the free-surface nonlinearity.

Appendix A. Numerical series for $B_{k1,j1}$, $B_{k(L_1+1)j1} B_{k1j(L_1+1)}$, and $B_{k(L_1+1)j(L_1+1)}$

Using asymptotic formulas (27) for the i-index numerical series in Eq. (16) associated with $B_{k\,1,j\,1}$, $B_{j(L_1+1),k1} = B_{k1,j(L_1+1)}$, and $B_{k(L_1+1),j(L_1+1)}$ shows that

$$\frac{c_{k1}^{(i)}c_{j1}^{(i)}}{\tanh(k_i)k_i N_i} - \frac{2\overline{h}\sqrt{\varDelta'_k\varDelta'_j}}{\pi i^2}\cos(b_k i)\cos(b_j i)\cos\left(a_k i - \frac{1}{4}\pi\right)\cos\left(a_j i - \frac{1}{4}\pi\right) = O(i^{-3}), \tag{A.1a}$$

$$\frac{c_{k1}^{(i)}c_{j(L_1+1)}^{(i)}}{\tanh(k_i)k_i N_i} + \frac{2\overline{h}\sqrt{\varDelta'_k\varDelta'_j}}{\pi i^2}\cos(b_k i)\sin(b_j i)\cos\left(a_k i - \frac{1}{4}\pi\right)\sin\left(a_j i - \frac{1}{4}\pi\right) = O(i^{-3}), \tag{A.1b}$$

$$\frac{c_{k(L_1+1)}^{(i)}c_{j(L_1+1)}^{(i)}}{\tanh(k_i)k_i N_i} - \frac{2\overline{h}\sqrt{\varDelta'_k\varDelta'_j}}{\pi i^2}\sin(b_k i)\sin(b_j i)\sin\left(a_k i - \frac{1}{4}\pi\right)\cos\left(a_j i - \frac{1}{4}\pi\right) = O(i^{-3}) \tag{A.1c}$$

as $i \to \infty$, where

$$a_p = \frac{\pi(z''_p - z'_p)}{2\overline{h}}, \quad b_p = \pi + \frac{\pi(z''_p + z'_p)}{2\overline{h}}, \quad p = 1, \dots, N.$$

Employing the Fourier-series representation of the (2π)−periodic functions presented in [17], we realize that

$$F(x) = \sum_{i=1}^{\infty} \frac{\cos(ix)}{i^2} = \frac{\pi^2}{6} - \frac{\pi x}{2} + \frac{x^2}{4}, \quad 0 \le x \le 2\pi, \tag{A.2a}$$

$$G(x) = \sum_{i=1}^{\infty} \frac{\sin(ix)}{i^2} = \frac{1}{2}\int_0^x \ln\left(\frac{1}{2(1-\cos t)}\right)dt = \frac{1}{2}\int_0^x \ln\left(\frac{t^2}{2(1-\cos t)}\right)dt - x(\ln|x|-1), \quad -\pi \le x \le \pi. \tag{A.2b}$$

This means that one can analytically find the infinite sums by the $O(1/i^2)$-dominating component in expressions (A.1), namely,

$$\sum_1^{k,j} = \frac{2\overline{h}}{\pi}\sqrt{\varDelta'_k\varDelta'_j}\sum_{i=1}^{\infty}\frac{1}{i^2}\cos(b_k i)\cos(b_j i)\cos\left(a_k i - \frac{1}{4}\pi\right)\cos\left(a_j i - \frac{1}{4}\pi\right) = \frac{\overline{h}}{4\pi}\sqrt{\varDelta'_k\varDelta'_j}[g_{kj}^{22} - g_{kj}^{11} + g_{kj}^{21} - g_{kj}^{12} + f_{kj}^{22} + f_{kj}^{11} + f_{kj}^{21} + f_{kj}^{12}], \tag{A.3a}$$

$$\sum_2^{k,j} = -\frac{2\overline{h}}{\pi}\sqrt{\varDelta'_k\varDelta'_j}\sum_{i=1}^{\infty}\frac{1}{i^2}\cos(b_k i)\sin(b_j i)\cos\left(a_k i - \frac{1}{4}\pi\right)\sin\left(a_j i - \frac{1}{4}\pi\right) = -\frac{\overline{h}}{4\pi}\sqrt{\varDelta'_k\varDelta'_j}[-g_{kj}^{22} - g_{kj}^{11} + g_{kj}^{21} + g_{kj}^{12} - f_{kj}^{22} + f_{kj}^{11} + f_{kj}^{21} - f_{kj}^{12}], \tag{A.3b}$$

$$\sum_{3}^{k,j} = \frac{2\overline{h}}{\pi}\sqrt{\Delta'_k\Delta'_j}\sum_{i=1}^{\infty}\frac{1}{i^2}\sin(b_k i)\sin(b_j i)\sin\left(a_k i - \frac{1}{4}\pi\right)\sin\left(a_j i - \frac{1}{4}\pi\right) = \frac{\overline{h}}{4\pi}\sqrt{\Delta'_k\Delta'_j}[g_{kj}^{22}-g_{kj}^{11}-g_{kj}^{21}+g_{kj}^{12}+f_{kj}^{22}+f_{kj}^{11}-f_{kj}^{21}-f_{kj}^{12}],$$

(A.3c)

where

$$g_{kj}^{22} = G\left(\frac{\pi}{\overline{h}}(\overline{z}''_k+\overline{z}''_j)\right),\quad g_{kj}^{11} = G\left(\frac{\pi}{\overline{h}}(\overline{z}'_k+\overline{z}'_j)\right),$$

$$g_{kj}^{21} = G\left(\frac{\pi}{\overline{h}}(\overline{z}''_k-\overline{z}'_j)\right),\quad g_{kj}^{12} = G\left(\frac{\pi}{\overline{h}}(\overline{z}'_k-\overline{z}''_j)\right),$$

$$f_{kj}^{22} = F\left(\frac{\pi}{\overline{h}}(\overline{z}''_k-\overline{z}''_j)\right),\quad f_{kj}^{11} = F\left(\frac{\pi}{\overline{h}}(\overline{z}'_k-\overline{z}'_j)\right),$$

$$f_{kj}^{21} = F\left(\frac{\pi}{\overline{h}}(\overline{z}''_k+\overline{z}'_j)\right),\quad f_{kj}^{12} = F\left(\frac{\pi}{\overline{h}}(\overline{z}'_k+\overline{z}''_j)\right).$$

Replacing the expressions for the considered matrix elements as

$$B_{k1,j1} = -\frac{c_{k1}^{(0)}c_{j1}^{(0)}}{\tan(k_0)k_0 N_0} + \sum_{1}^{k,j} + \sum_{i=1}^{\infty}\left[\frac{c_{k1}^{(i)}c_{j1}^{(i)}}{\tanh(k_i)k_i N_i} - \frac{2\overline{h}\sqrt{\Delta'_k\Delta'_j}}{\pi i^2}\cos(b_k i)\cos(b_j i)\cos\left(a_k i - \frac{1}{4}\pi\right)\cos\left(a_j i - \frac{1}{4}\pi\right)\right],$$
(A.4a)

$$B_{k1,j(L_1+1)} = -\frac{c_{k1}^{(0)}c_{j(L_1+1)}^{(0)}}{\tan(k_0)k_0 N_0} + \sum_{2}^{k,j} + \sum_{i=1}^{\infty}\left[\frac{c_{k1}^{(i)}c_{j(L_1+1)}^{(i)}}{\tanh(k_i)k_i N_i} + \frac{2\overline{h}\sqrt{\Delta'_k\Delta'_j}}{\pi i^2}\cos(b_k i)\sin(b_j i)\cos\left(a_k i - \frac{1}{4}\pi\right)\sin\left(a_j i - \frac{1}{4}\pi\right)\right],$$
(A.4b)

$$B_{k(L_1+1),j(L_1+1)} = -\frac{c_{k(L_1+1)}^{(0)}c_{j(L_1+1)}^{(0)}}{\tan(k_0)k_0 N_0} + \sum_{3}^{k,j} + \sum_{i=1}^{\infty}\left[\frac{c_{k(L_1+1)}^{(i)}c_{j(L_1+1)}^{(i)}}{\tanh(k_i)k_i N_i} - \frac{2\overline{h}\sqrt{\Delta'_k\Delta'_j}}{\pi i^2}\sin(b_k i)\sin(b_j i)\sin\left(a_k i - \frac{1}{4}\pi\right)\sin\left(a_j i - \frac{1}{4}\pi\right)\right]$$
(A.4c)

provides the $O(i^{-3})$-terms in the square brackets of (A.4). This means that taking K elements of these numerical series leads to the $O(1/K^2)$-order error.

References

[1] H. Abramson, The Dynamic Behavior of Liquids in Moving Containers, Washington DC, NASA SP-106, 1966.

[2] O.M. Faltinsen, A.N. Timokha, *Sloshing*, Cambridge University Press, 2009.

[3] M.J. Tait, A.A. El Damatty, N. Isyumov, M.R. Siddique, Numerical flow models to simulate tuned liquid dampers (TLD) with slat screens, *Journal of Fluids and Structures* 20 (2005) 1007–1023.

[4] O.M. Faltinsen, R. Firoozkoohi, A.N. Timokha, Analytical modeling of liquid sloshing in a two-dimensional rectangular tank with a slat screen, *Journal of Engineering Mathematics*, in press, doi:10.1007/s10665-010-9397-5.

[5] R. Porter, D.V. Evans, Complementary approximations to wave scattering by vertical barriers, *Journal of Fluid Mechanics* 294 (1995) 155–180.

[6] I. Gavrilyuk, I. Lukovsky, Yu. Trotsenko, A. Timokha, Sloshing in a vertical circular cylindrical tank with an annular baffle. Part 1. Linear fundamental solutions, *Journal of Engineering Mathematics* 54 (2006) 71–88.

[7] O.M. Faltinsen, O.F. Rognebakke, A.N. Timokha, Two-dimensional resonant piston-like sloshing in a moonpool, *Journal of Fluid Mechanics* 575 (2007) 359–397.

[8] R. Firoozkoohi, O.M. Faltinsen, R. Experimental and numerical investigation of the effect of swash bulkhead on sloshing. *ISOPE2010, Proceedings of the Twentieth (2010) International Offshore (Ocean) and Polar Engineering Conference*, Beijing, China, June 20–26, 2010.

[9] R.D. Blevins, *Applied Fluid Dynamics. Handbook*, Krieger, Malabar, FL, 1990.

[10] J.-P. Morand, R. Ohayon, *Fluid Structure Interaction. Applied Numerical Methods*, John Wiley & Sons, Chichester, New York, Brisbane, Toronto, Singapore, 1995.

[11] L.M. Milne-Thompson, *Theoretical Hydrodynamics*, fifth ed., Dover, 1968.

[12] T. Erdélyi, W.B. Johnson, The "full Müntz theorem" in $L_p[0,1]$ for $0 < p < \infty$, *Journal of Analytical Mathematics* 84 (2001) 145–172.

[13] G.N. Watson, *A Treatise on the Theory of Bessel Functions*, Cambridge University Press, 1995.

[14] D.V. Evans, P. McIver, Resonant frequencies in a container with vertical baffles, *Journal of Fluid Mechanics* 175 (1987) 295–305.

[15] R. Jeyakumaran, P. McIver, Approximations to sloshing frequencies for rectangular tanks with internal structures, *Journal of Engineering Mathematics* 29 (1995) 537–556.

[16] E.O. Tuck, The effect of a submerged barrier on the natural frequencies and radiation damping of a shallow basin connected to open water, *Journal of the Australian Mathematical Society B* 22 (1980) 104–128.

[17] I.S. Gradshtein, I.M. Ryzhik, *Tables of Integrals Series and Products*, fourth ed., Academic, New York, 1965.